**Supporting Information**

# P-N-P Bridge Bond Engineering in Black Phosphorus Overcomes Phosphorus Redox Reaction Kinetic Barriers for Fast-charging Lithium Batteries

*Yibo Ma [1,2,3], Kai Wang [1,4*], Kewei Liu [1], Yang Guo [1], Yanan Xu [1,4], Xianzhong Sun [1,4], Xiong Zhang [1,4], Lingfeng Zhu [2,3], Haimei Xu [2,3], Yanwei Ma [1,4,5*], Tianyi Ma [2,3*]*

[1] Institute of Electrical Engineering, Chinese Academy of Sciences, Beijing, 100190, China

[2] Centre for Atomaterials and Nanomanufacturing (CAN), School of Science, RMIT University, Melbourne, VIC 3000, Australia

[3] ARC Industrial Transformation Research Hub for Intelligent Energy Efficiency in Future Protected Cropping (E2Crop), Melbourne, VIC 3000, Australia

[4] School of Engineering Sciences, University of Chinese Academy of Sciences, Beijing, 100049, China

[5] School of Materials Science and Engineering, Zhengzhou University, Zhengzhou 450001, P. R. China

Correspondence author*, e-mail: wangkai@mail.iee.ac.cn, ywma@mail.iee.ac.cn, tianyi.ma@rmit.edu.au.

**Supplementary Note**

The ball milling process generates substantial mechanical energy through severe collisions, can induce localized regions with temperatures exceeding 200°C and pressures surpassing 6 GPa 3. Under these conditions, the weak P-N bonds in the original P3N5 reactant and the P-P bonds in the BP layer are likely to break, producing free nitrogen components and phosphorus defects, as illustrated in **Fig. S1**.

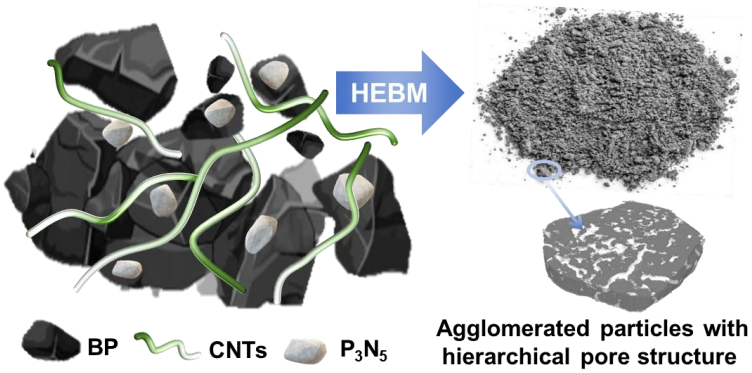


**Supplementary Fig. S1** Schematic diagram of ball milling process.

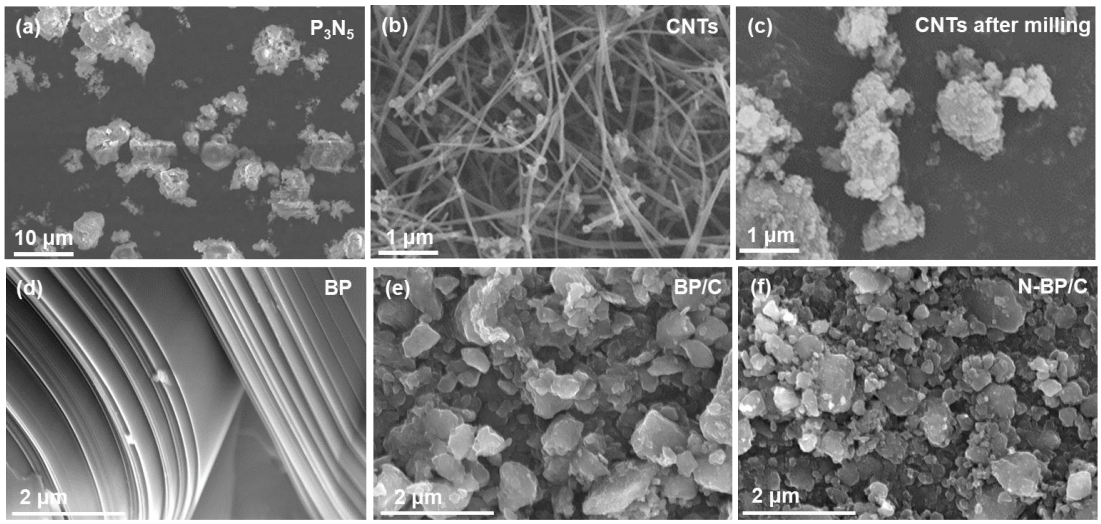


**Supplementary Fig. S2** The morphologies of the precursors of (a) P3N5 and (b) CNTs before HEBM process, (c) CNTs derived carbon after HEBM, (d) layered BP before HEBM, agglomerated particles of (e) BP/C and (f) N-BP/C.

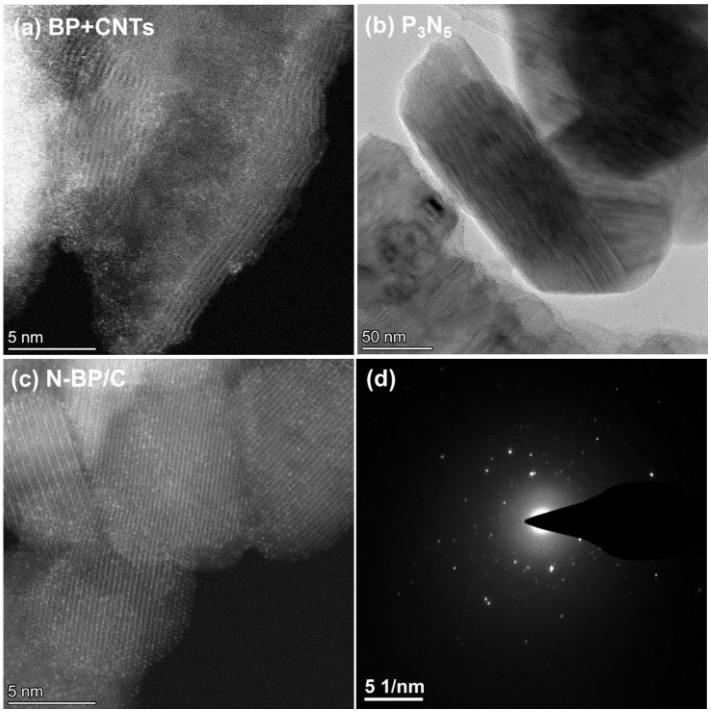


**Supplementary Fig. S3** The evolution of microstructures, (a) the layered structure of physically mixed BP+CNTs powders and (b) the original P3N5 particle before HEBM, (c) agglomeration of the crystalline grains with different orientations and (d) the corresponding selected area electron diffraction (SAED) together illustrate the polycrystalline structure after HEBM process.

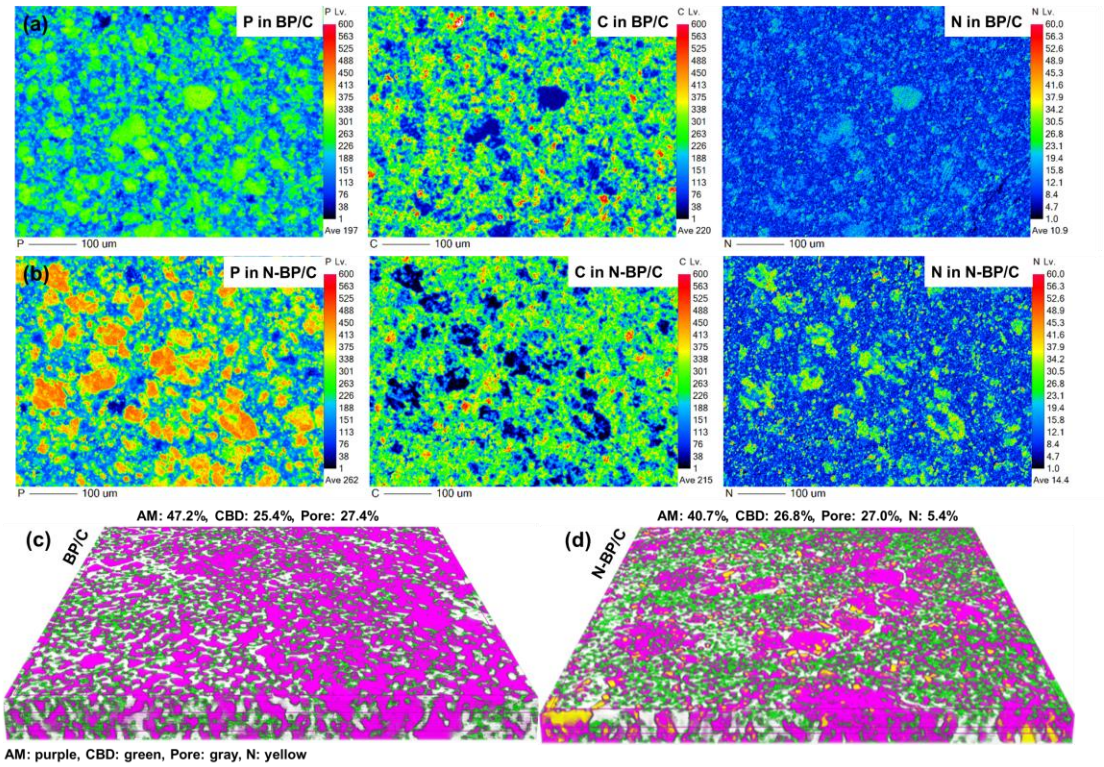


**Supplementary Fig. S4** Surface distribution of the P, C and N elements on the (a) BP/C electrode and (b) N/BP/C electrode, measured by EPMA; bulk distribution of different electrode compositions in (c) BP/C electrode and (d) N-BP/C electrode, measured by nano-CT (AM: active materials, CBD: conductive carbons and binders, Pore: the pores and holes between different particles).

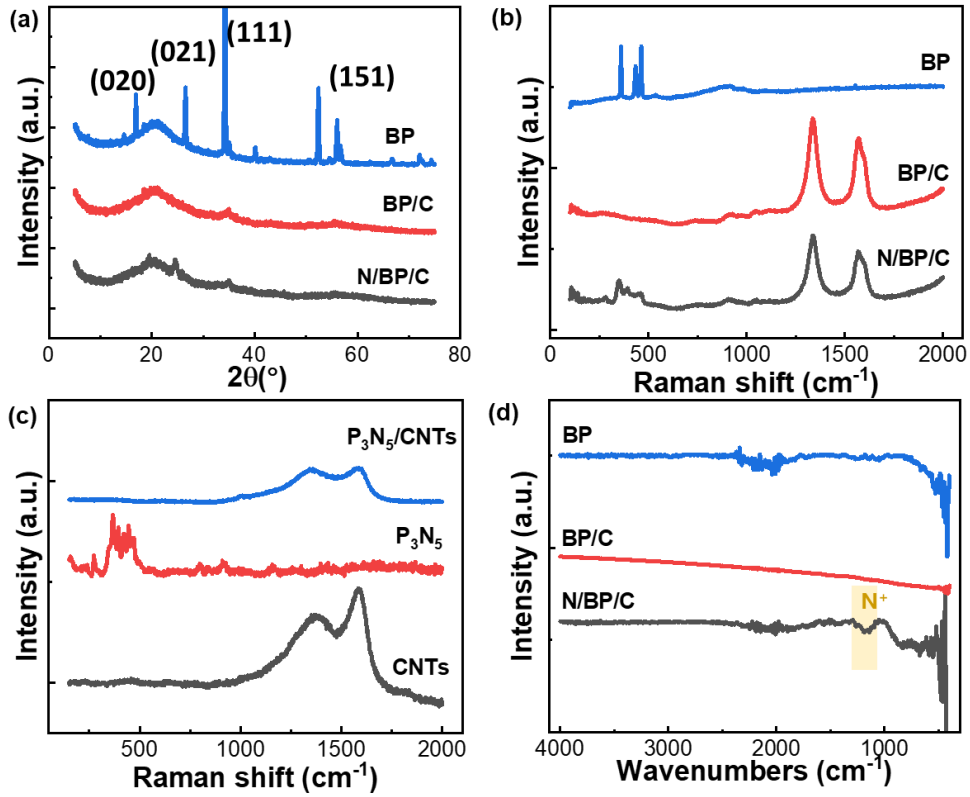


**Supplementary Fig. S5** (a) XRD patterns, (b, c) Raman spectra, (d) FTIR curves.

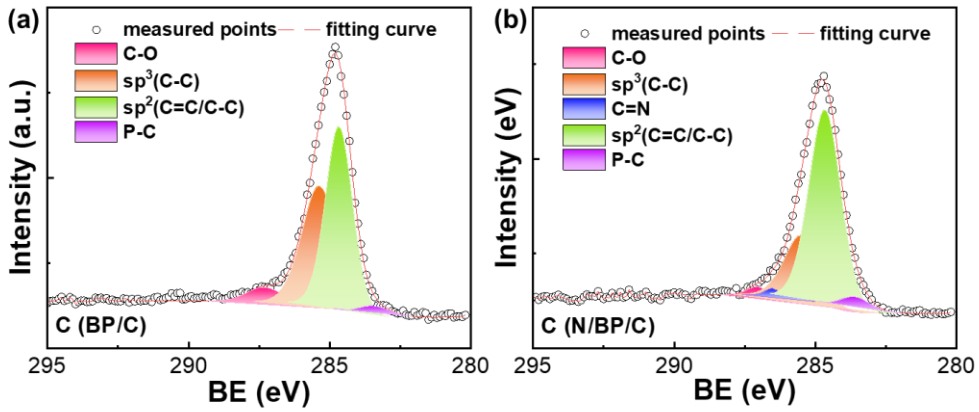


**Supplementary Fig. S6** Comparison of C 1s XPS spectra in (a) BP/C and (b) N-BP/C samples.

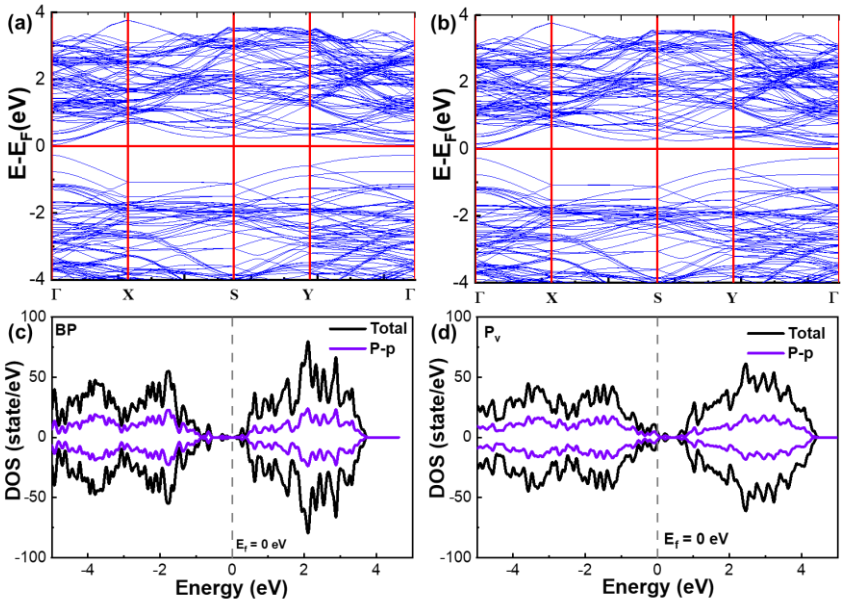


**Supplementary Fig. S7** Band structure and density of states (DOS) of (a, c) original BP structure and (b, d) special vacancies in BP layer (Pv), the decreased band gap and the non-zero PDOS at Fermi level together imply the metallic state.

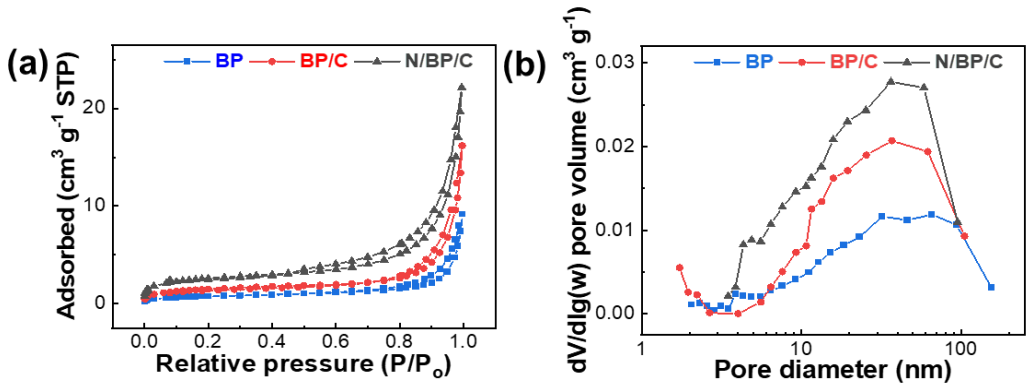


**Supplementary Fig. S8** (a) N2 adsorption/desorption isotherms, (b) pore size distribution based on BJH model.

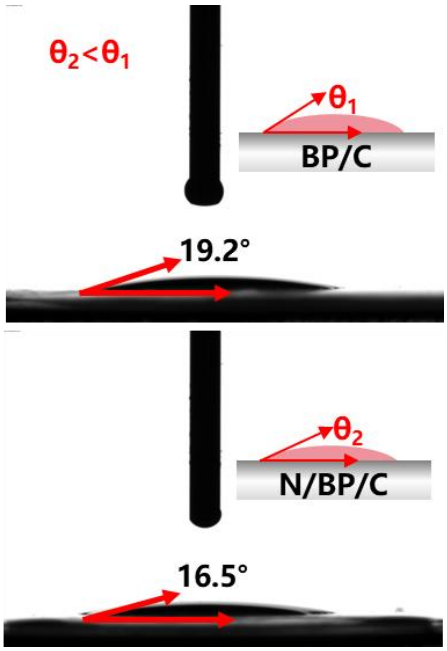


**Supplementary Fig. S9** Contact angle testing.

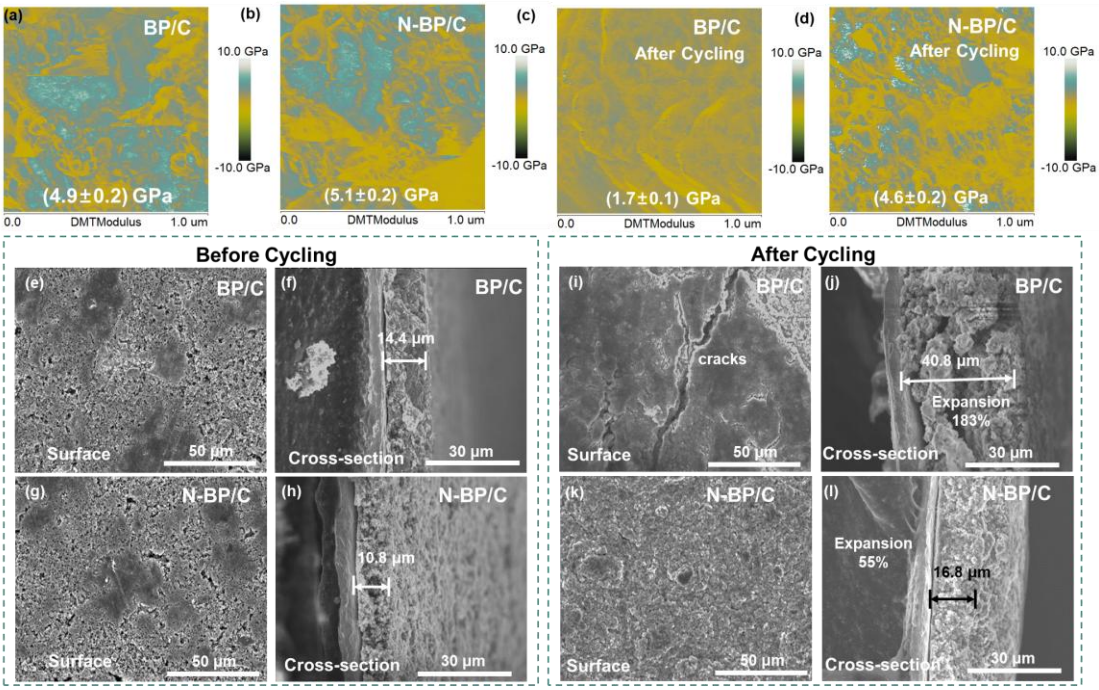


**Supplementary Fig. S10** Structural stability of BP-based negative electrode, (a-d) improved Young's modulus, (e-l) surface and cross-section images of BP-based electrodes during charge-discharge process.

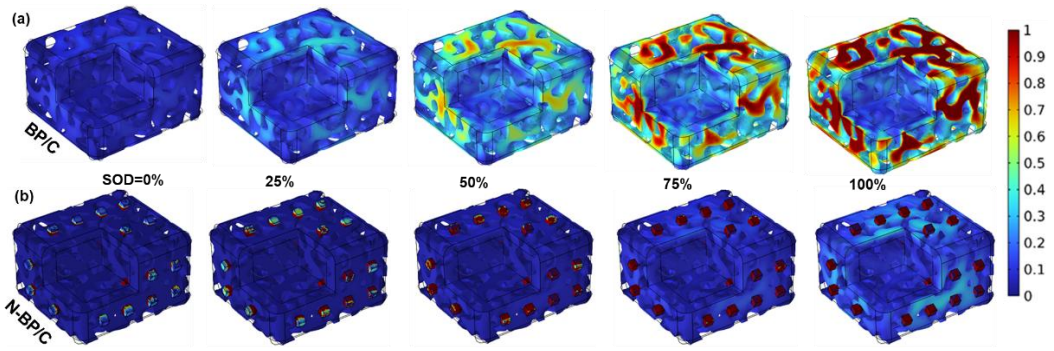


**Supplementary Fig. S11** The distribution of induced stress under different states of discharge (SOD) in the (a) BP/C and (b) N-BP/C agglomeration particle models by Comsol software.

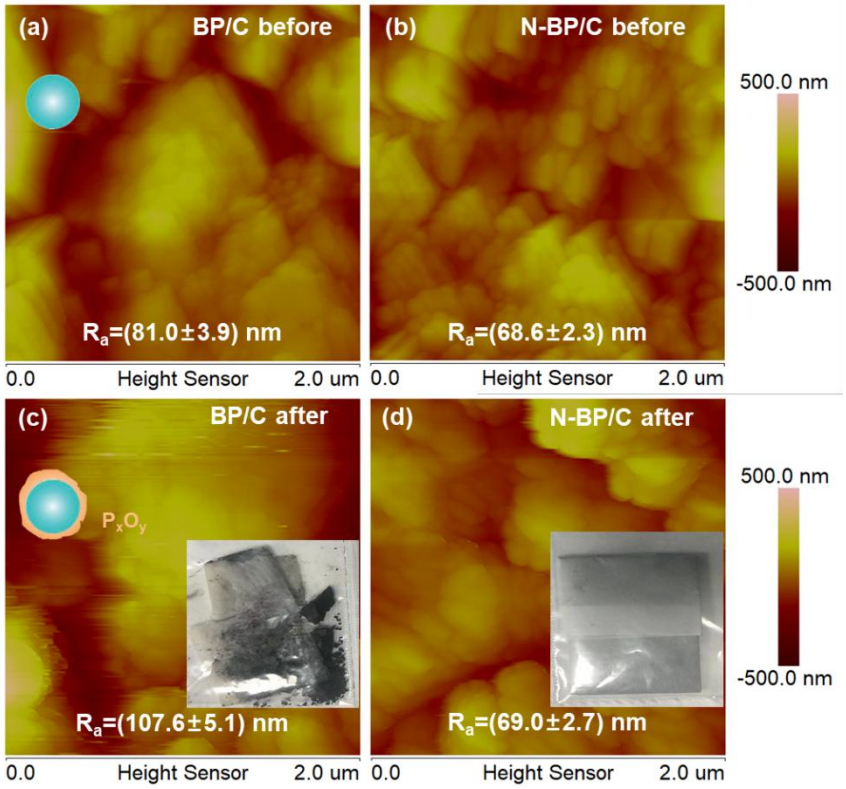


**Supplementary Fig. S12** Air stability experiments, the measured surface morphology and roughness of (a, c) BP/C and (b, d) N-BP/C electrodes before/after exposure to air atmosphere.

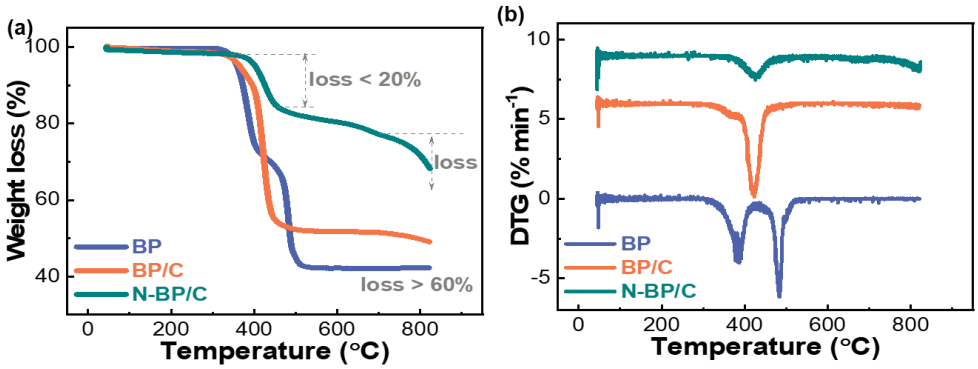


**Supplementary Fig. S13** Thermal stability experiments, thermograms of the pure BP, BP/C and N-BP/C composites, (a) TG, (b) DTG.

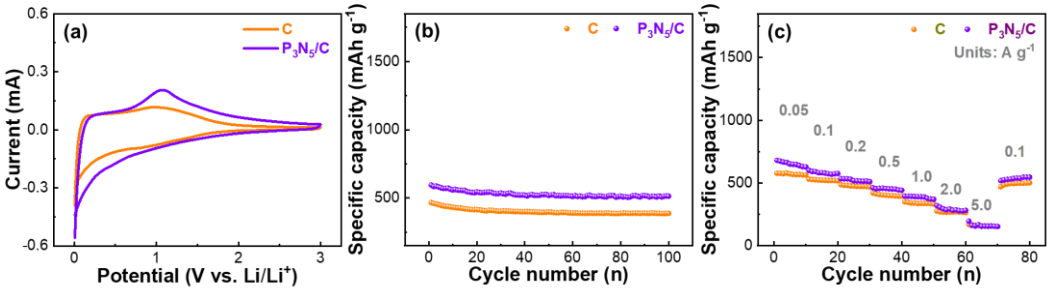


**Supplementary Fig. S14** Supplement of the (a) CV, (b) cycle and (c) rate performance of the carbons obtained by pure CNTs after HEBM and the P3N5/C composite after HEBM, these two composites are important to exclude the increase of capacity caused by N doping in carbons or the extra capacity provided by changed carbon materials.

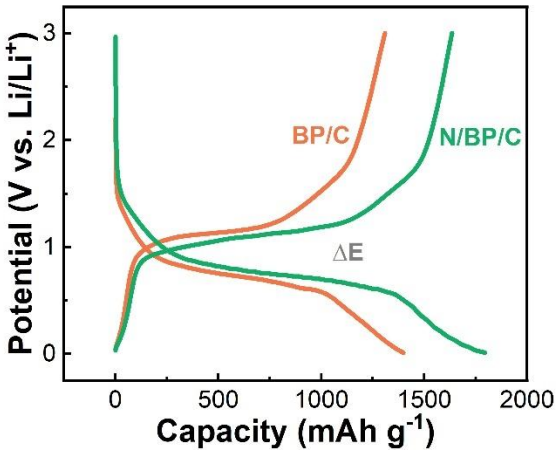


**Supplementary Fig. S15** The charge/discharge curves of BP/C and N/BP/C measured with the same voltage range of 0.01~3.0 V vs $Li^+$/Li, and the calculated polarization voltage △E.

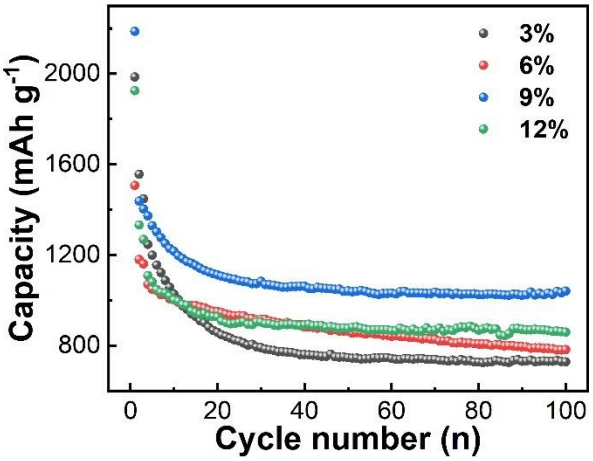


**Supplementary Fig. S16** Comparison of the cycle performance with different N contents, 3%, 6%, 9% and 12%.

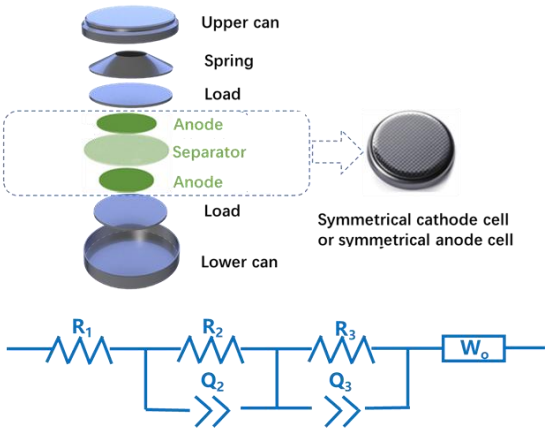


**Supplementary Fig. S17** Schematic diagram of symmetrical battery and its equivalent circuit diagram.

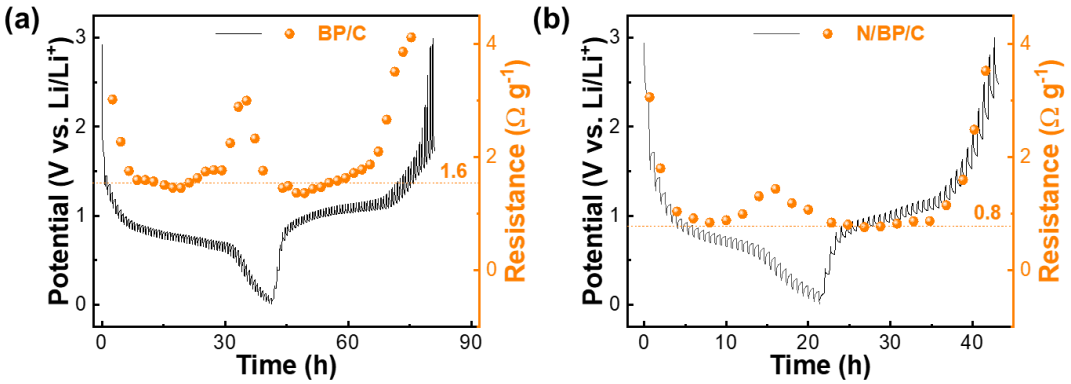


**Supplementary Fig. S18** The calculated Li-ions transport resistance based on the GITT data, (a) BP/C electrode, (b) N-BP/C electrode.

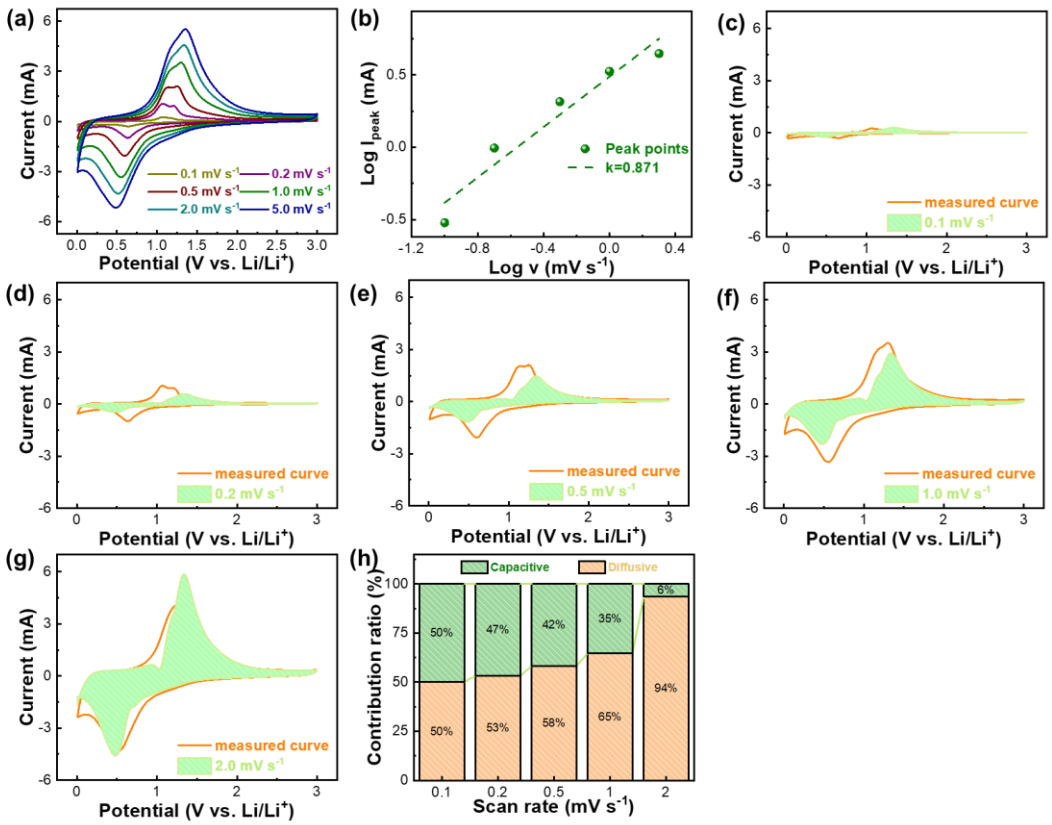


**Supplementary Fig. S19** Capacitive contribution of N-BP/C anode. (a, b) CV curves measured at different scan rates of N/BP/C and the calculated slope. The calculated capacitive contribution (green area) to the overall Li-ions storage at (c) 0.1, (d) 0.2, (e) 0.5, (f) 1.0 and (g) 2.0 mV s-1. (h) The capacity from the diffusion-controlled (represented by the height of green columns) and the capacitive process (represented by the height of yellow columns). The values in columns are the ratio of each part to the overall capacity.

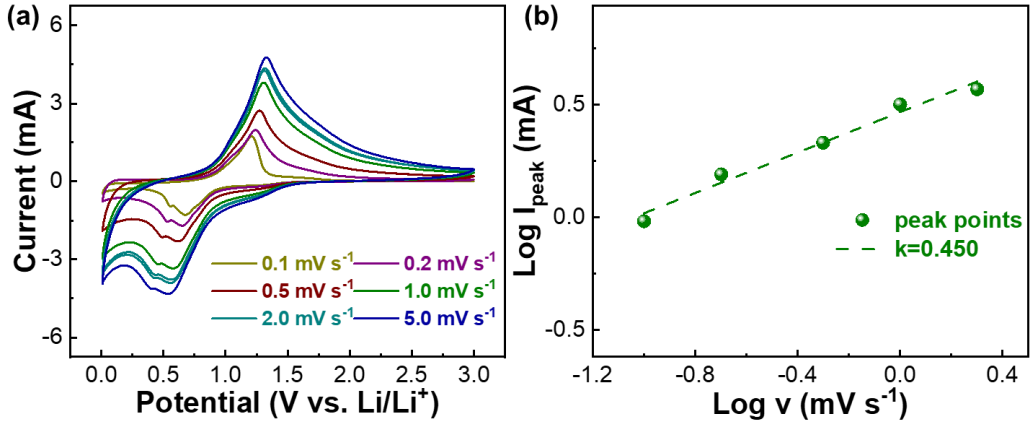


**Supplementary Fig. S20** Capacitive contribution of BP/C anode. (a) CV curves measured at different scan rates and (b) the calculated slope.

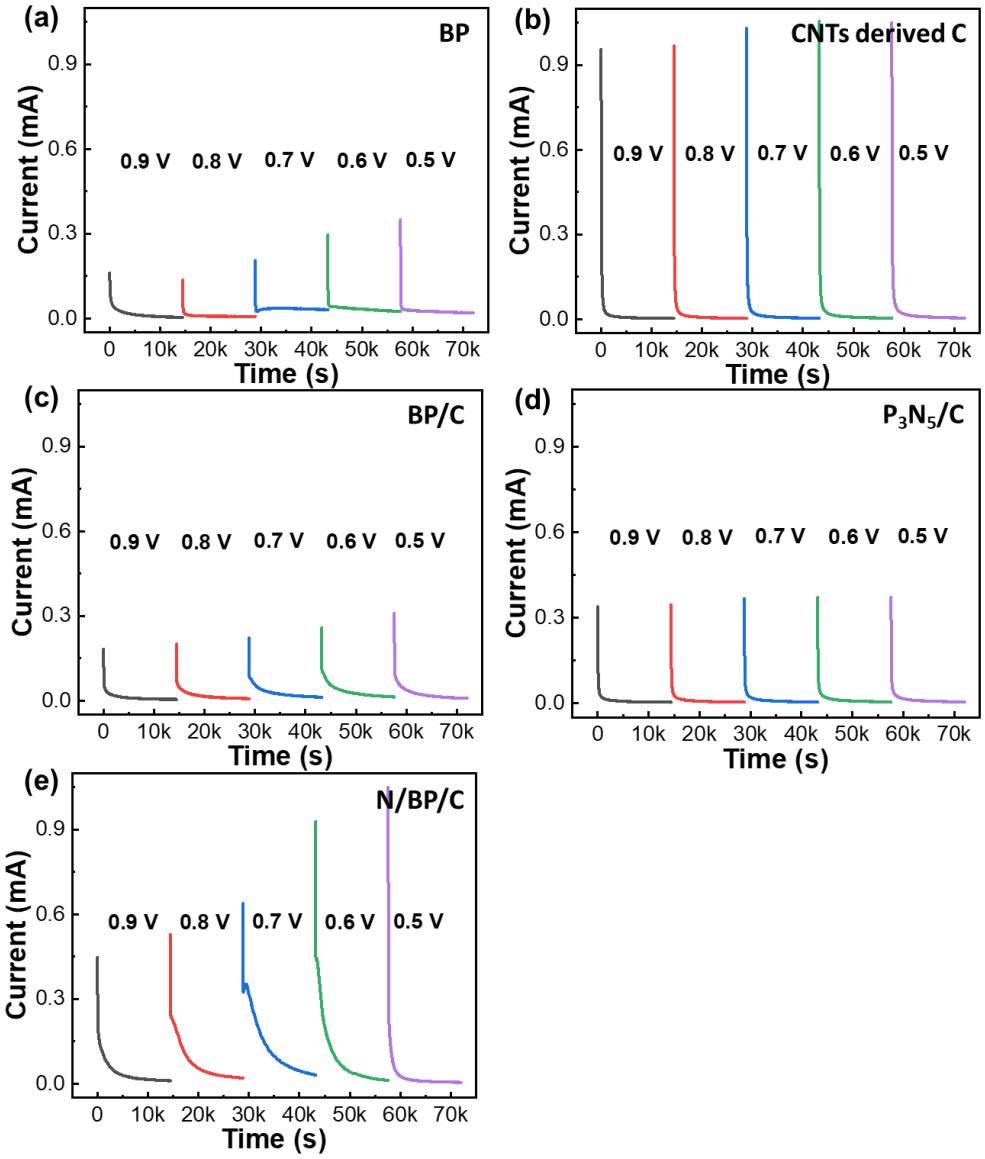


**Supplementary Fig. S21** Deposition experiments performed with the constant current-constant voltage (CCCV) discharge mode, the half-cells were discharged with a constant current of 0.5 A g-1 to the target voltage and continuously discharged at the constant voltage until the current decreases to 0.1 A g-1, all discharge process performed with a voltage step of 0.1 V. Five different half-cells are measured (a) BP, (b) CNTs derived carbon, (c) BP/C, (d) P3N5/C and (e) N-BP/C.

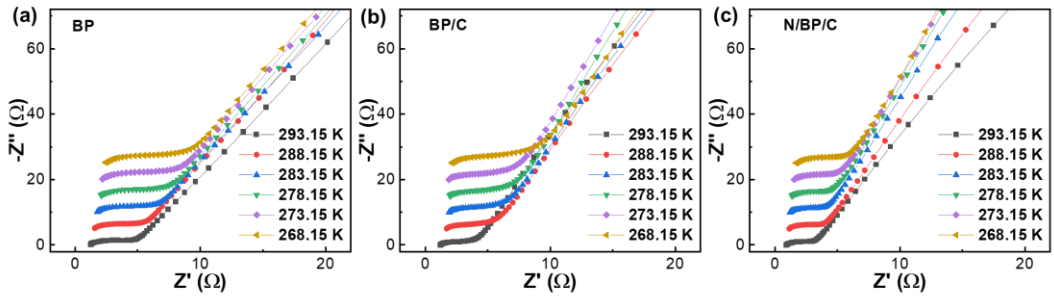


**Supplementary Fig. S22** EIS measurements of symmetric cells, (a) BP, (b) BP/C and (c) N-BP/C. Each measurement was performed at various temperatures of 268.15 K~293.15 K.

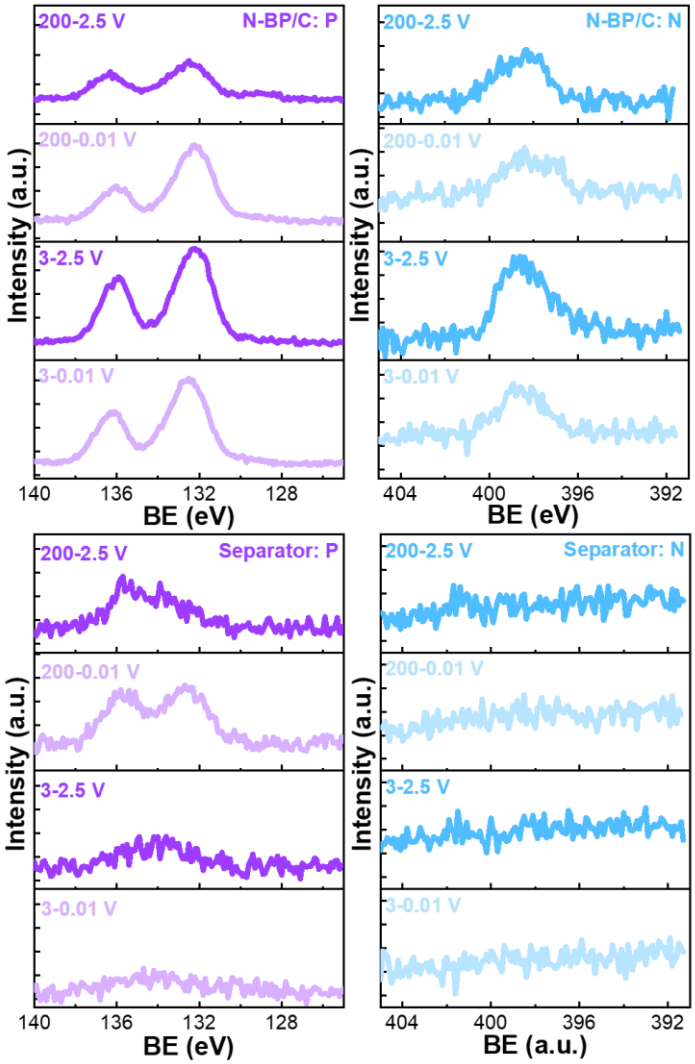


**Supplementary Fig. S23** Stable P 2p and N 1s signals on N-BP/C electrode and separator, measured by XPS during discharging/charging process.

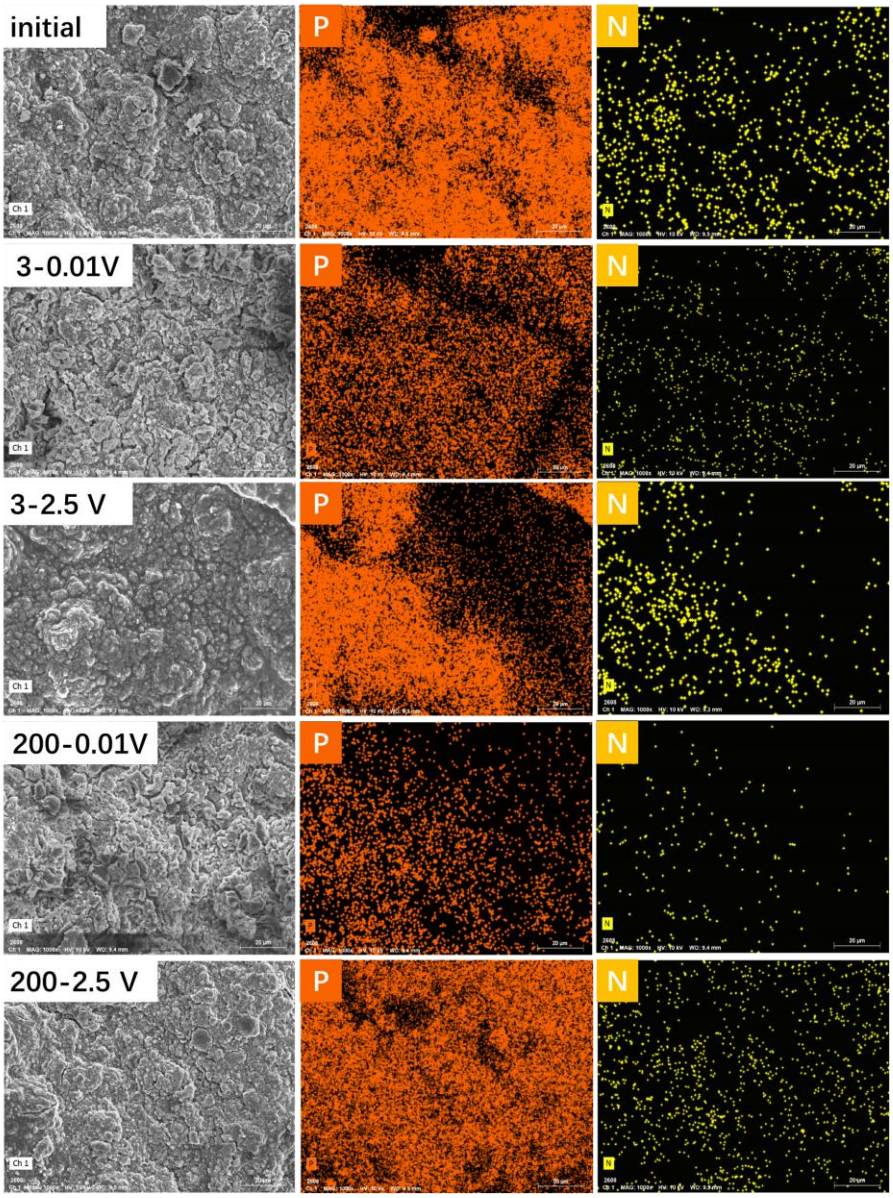


**Supplementary Fig. S24** Reversible P and N signals of N-BP/C electrode measured by EDS during discharging/charging process.

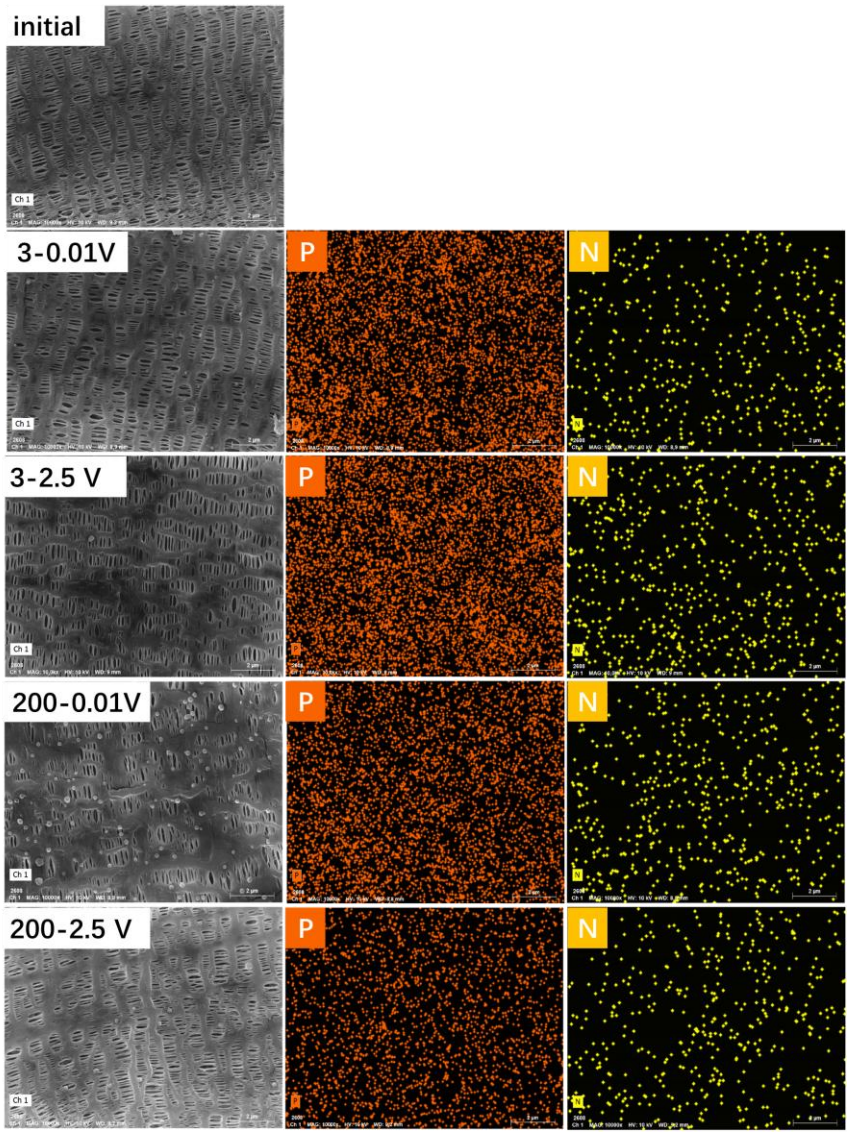


**Supplementary Fig. S25** Reversible P and N signals of separator measured by EDS during discharging/charging process.

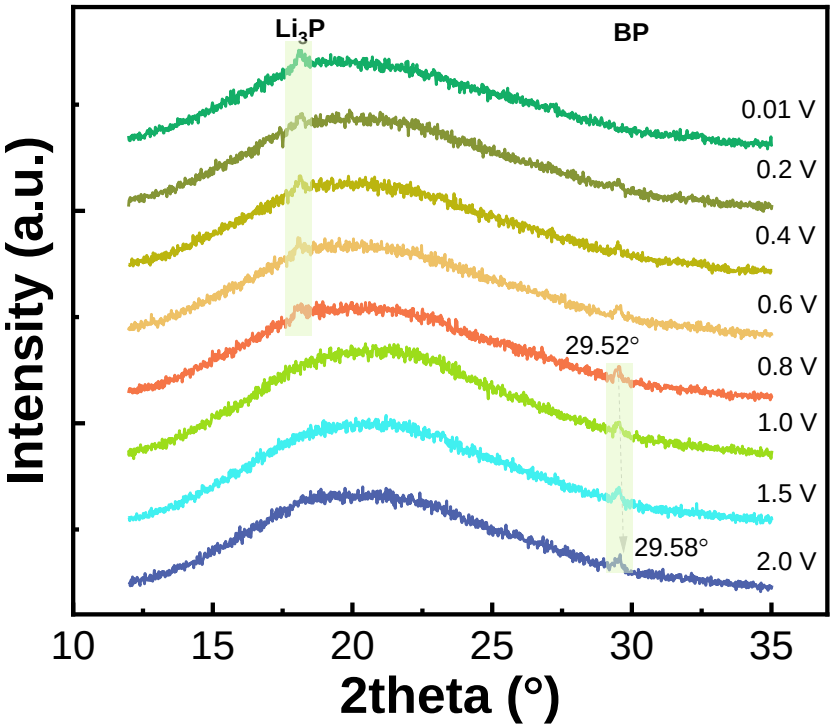


**Supplementary Fig. S26** XRD results during initial discharge process.

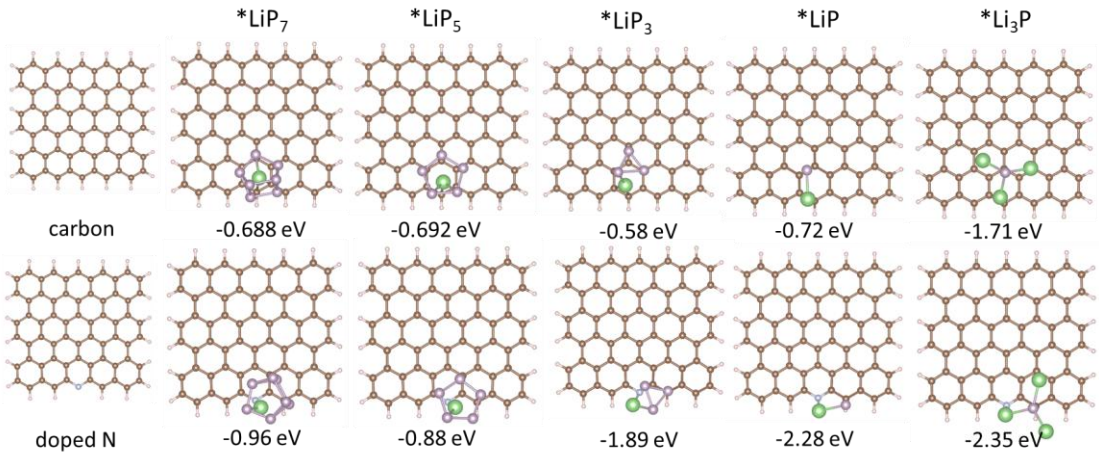


**Supplementary Fig. S27** Adsorption energies of LiPx on the bare carbon layer and N modified carbon.

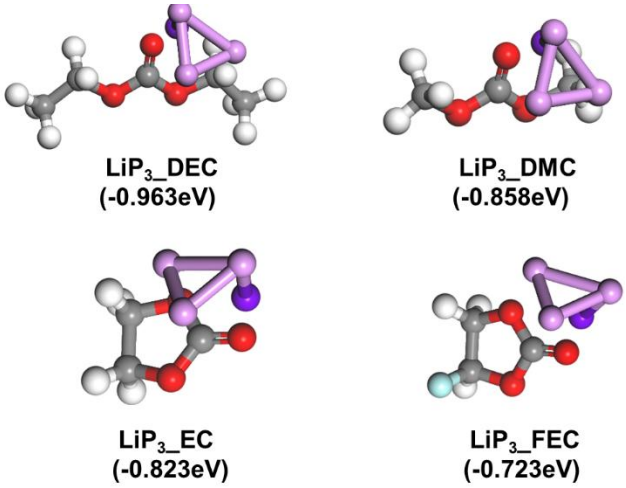


**Supplementary Fig. S28** The simulated solvation energy between the intermediate Lithium polyphosphate (LiP3) and the solvents EC, DEC, DMC and FEC in electrolyte.

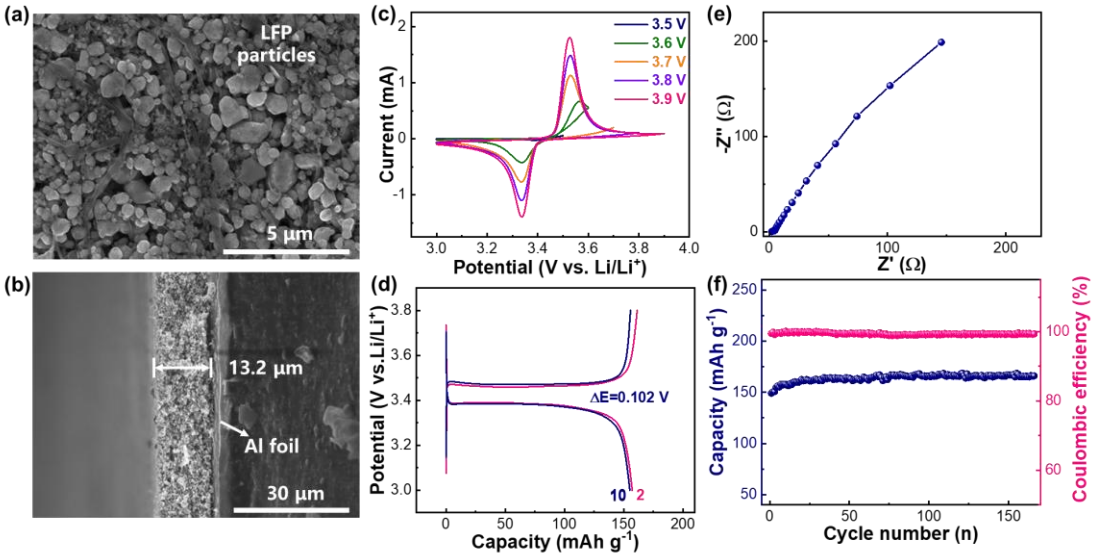


**Supplementary Fig. S29** The (a) surface and (b) cross-section morphologies of LiFePO4 cathodes, corresponding electrochemical performance of (c) CV, (d) charge/discharge curves, (e) EIS and (f) cycle performance.

Supported by empirical data, this catalysis study in phosphorus-based batteries achieved the most outstanding rate performance to date. Notably, its Imax × capacity was higher than that of the previously recorded highest value (**Table S1**), indicating that our work shows the best rate performance, it can recharge 80% energy of a battery less than 10 min, meeting the eXtreme Fast Charging (XFC) standards provided by U.S. Department of Energy.

**Table S1** Comparison with other phosphorus-based batteries.

| **Max current (A g-1)** | **capacity (Ah g-1)** | **Imax ×capacity (A2h g-2)** | **Fast-charge time (min)** | **Anode material** | **References** |
|---|---|---|---|---|---|
| 5 (1) | 1.25 (1.48) | 6.25 (1.48) | 9.5 | N-BP/C | This work |
| 13 (5.2) | 0.44 (0.79) | 5.72 (4.11) | none | (BP-G)/PANI | Science 370, 192-197 (2020) |
| 1 (0.2) | 1.09 (1.36) | 1.09 (0.27) | none | RP@CNF | Nature Communications 11, 2520 (2020) |
| 6 (1) | 0.11 (0.13) | 0.66 (0.13) | none | Oxidized BP/rGO | Nature Materials 18, 156-162 (2019) |
| 0.25 | 2.24 | 0.56 | none | BP@Graphite | Angew. Chem. Int. Ed. 59, 2318-2322 (2020) |
| 4 (0.2) | 0.48 (0.86) | 1.93 (0.17) | none | BP-G | Nature Nanotechnology 10, 980-985 (2015) |
| 5 (1) | 0.71 (0.93) | 3.55 (0.93) | none | RP@B-doped C | Energy Environ. Sci. 17, 4273-4282 (2024) |
| 5.2 (1.3) | 1.0 (1.2) | 5.2 (1.56) | > 9 | S/BP | J. Am. Chem. Soc. 146, 20700-20708 (2024) |
| 0.52 | 0.62 | 0.32 | none | BP@C | ACS A. M. Interfaces 14, 18506-18512 (2022) |
| 1.3 | 1.69 | 2.19 | none | COF@P/C | Adv. Mater. 35, 2208514 (2023) |
| 5 (1) | 0.45 (0.72) | 2.25 (0.72) | 14.7 | Sb@BP/C | Adv. Energy Mater. 14, 2304408 (2024) |

**Table S2** Comparison with other phosphorus-based batteries.

| **Max cycles** | **Current density (A g-)** | **Capacity retention ratio (%)** | **Full-cell material** | **References** |
|---|---|---|---|---|
| **>3400** | 1 | 92% | LiFePO4‖N-BP/C | This work |
| **300** | 15.6 | ~80% | S/BP‖LCO | J. Am. Chem. Soc. 146, 20700-20708 (2024) |
| **300** | 0.5 | 82.2% | LiFePO4@C ‖ RP-BG | Energy Environ. Sci. 17, 4273-4282 (2024) |
| **200** | 1.3 | 92% | NCM‖P-KB | Nano Energy 59, 464-471 (2019) |

## Reference


1. Huang P, Guo Z. Li-ion distribution and diffusion-induced stress calculations of particles using an image-based finite element method. *Mechanics of Materials* **157**, (2021).
2. Eshghinejad A, Li J. The coupled lithium ion diffusion and stress in battery electrodes. *Mechanics of Materials* **91**, 343-350 (2015).
3. Ma Y*, et al.* Black Phosphorus Covalent Bonded by Metallic Antimony Toward High-Energy Lithium-Ion Capacitors. *Advanced Energy Materials* **14**, (2024).
4. Ma Y*, et al.* Dehalogenation produces graphene wrapped carbon cages as fast-kinetics and large-capacity anode for lithium-ion capacitors. *Carbon* **202**, 175-185 (2023).